ACS Catalysis

pubs.acs.org/acscatalysis Research Article

Pd−Au−Cu Ternary Alloy Nanoparticles: Highly Tunable and Economical Nitrite Reduction Catalysts

Pranaw Kunal,[▽] Chenxu Yan,[▽] Hongyu Guo, Hao Li, Carolyn E. Brady, Michael Duncan, Xun Zhan, Charles J. Werth,* Graeme Henkelman,* and Simon M. Humphrey*

Cite This: *ACS Catal.* 2023, 13, 11945−11953 Read Online

ACCESS | Metrics & More | Article Recommendations | Supporting Information

ABSTRACT: Solid-solution ternary Pd−Au−Cu nanoparticles (NPs) with broadly tunable compositions ($Pd_xAu_yCu_{100-(x+y)}$; where x = 30−70 and y = 15−35) were prepared by a microwave-assisted polyol reduction method. Commercially available Pd^{2+}, Au^{3+}, and Cu^{2+} salts were directly co-reduced by ethylene glycol and $NaBH_4$ in a one-pot process to generate near-monodisperse ternary alloy NPs with mean sizes between 2 and 4 nm. Using the same synthetic approach, the corresponding binary alloy PdCu NPs with similar monodispersities and particle sizes were also prepared. The comparative catalytic performances of PdCu NPs and PdAuCu NPs were assessed for the aqueous-phase reduction of nitrate (NO_3^-) anions and were compared to previously published results for analogous binary PdAu NPs. The experimental catalytic results and theoretical studies reveal that the resulting catalytic activity of Pd surface sites are highly sensitive to the relative amounts of Au and Cu also present. We ultimately prove that the hitherto unstudied ternary PdAuCu NPs are highly active and selective as NO_2^- reduction catalysts and effectively utilize Cu as an economically viable dilutant metal, without sacrificing the activity or stability of industrially important and well-studied PdAu alloy catalysts. From an economic perspective, the ternary alloy nanocatalysts show superior price-to-activity ratios: the measured turnover rates of $Pd_{63}Au_{22}Cu_{16}$ NPs (3.353 min^{-1} $\$^{-1}$) outperform not only monometallic Pd NPs (0.797 min^{-1} $\$^{-1}$) but also binary PdAu NPs and PdCu NPs of all accessible compositions.

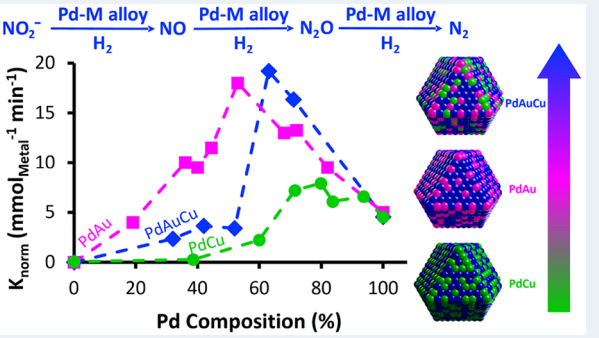

KEYWORDS: *microwave synthesis, alloy nanoparticles, palladium−gold−copper alloys, palladium−copper alloys, density functional theory, nitrite reduction, composition-dependent catalytic tunability*

INTRODUCTION

Nitrate (NO_3^-) is the most ubiquitous groundwater contaminant in the United States.[1] Prominent sources of NO_3^- arise from the use of fertilizers, livestock, and septic systems.[2,3] Consumption of NO_3^--contaminated water can be especially fatal to infants, causing methemoglobinemia or "blue baby syndrome".[4,5] Therefore, the U.S. Environmental Protection Agency (EPA) established a maximum contaminant level of 10 mg L^{-1} (as N) for NO_3^-. Nitrite (NO_2^-) is the first reduction intermediate of NO_3^-, having an oxidation state of N(III). It has shown greater acute toxicity than its N(V) precursor and can produce carcinogenic *N*-nitroso compounds in the human body.[6] Due to the abundance of NO_3^- in drinking water that can act as a source of more highly toxic NO_2^-, the permissible level of NO_2^- is more stringently regulated, with a maximum contaminant level of 1 mg L^{-1} (as N). Therefore, catalytic reduction of NO_3^- and NO_2^- continues to gain increasing attention as a promising water treatment technology. Catalytic denitrification offers obvious advantages over current processes (*e.g.*, biological treatment, reverse osmosis membrane separation, or ion exchange), which include fast kinetics, ease of operation, low energy consumption, and minimization of secondary waste disposal.[2,7] As shown in the proposed catalytic reaction pathways (Scheme 1), a metal species that is capable of H_2 activation is required throughout the NO_2^- reduction processes; platinum group

Scheme 1. Proposed Reaction Pathways for Catalytic Nitrite Reduction with Pd-Based Alloys

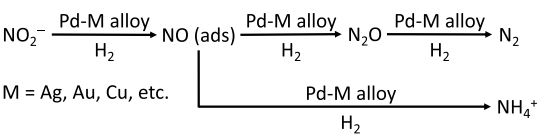

Received: April 12, 2023
Revised: July 14, 2023

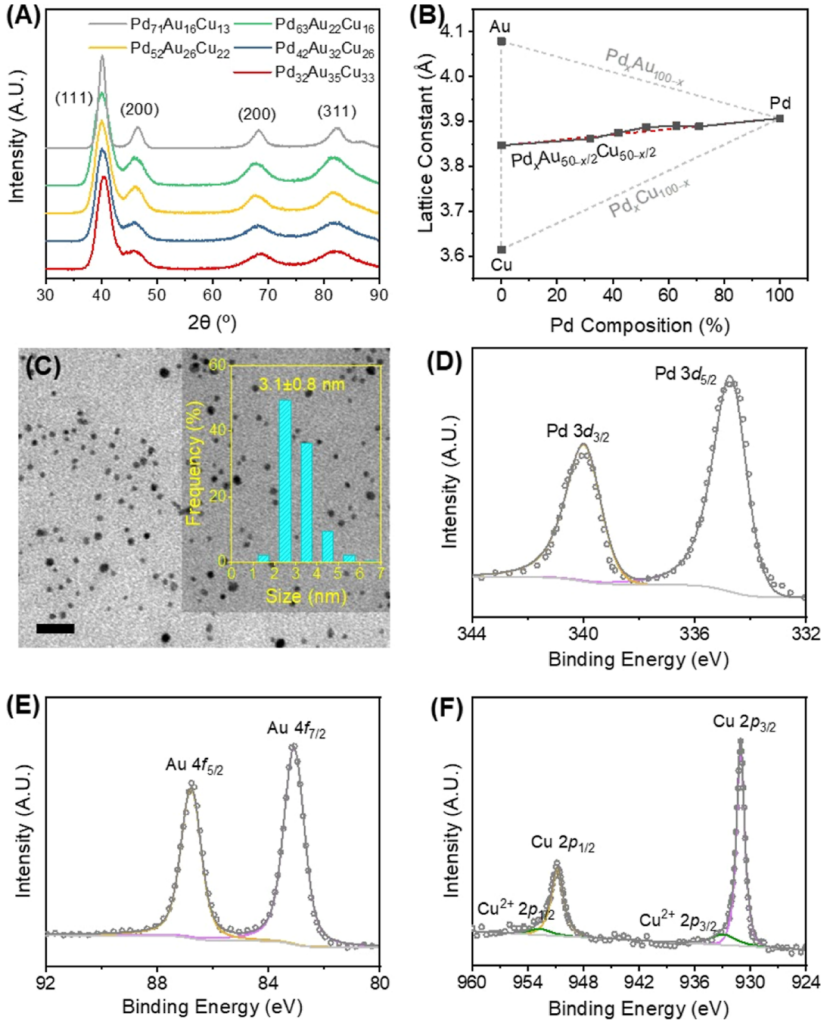

Figure 1. (A) PXRD patterns of PdAuCuNPs with various compositions. (B) Vegard's plot showing lattice constants of $Pd_xAu_{50-x/2}Cu_{50-x/2}$NPs as a function of Pd composition. (C) TEM image of $Pd_{52}Au_{26}Cu_{22}$NPs. Scale bar is 20 nm. Inset: size distribution histograph. (D) Pd 3d, (E) Au 4f, and (F) Cu 2p XPS spectra of $Pd_{52}Au_{26}Cu_{22}$NPs.

metals are most commonly used for this purpose. Metallic Pd catalysts have gained considerable attention in this field over the past decade: numerous Pd-based catalysts including Pd-based alloys like Pd−Ag and Pd−Au have been reported to display superior catalytic performances compared to other platinum group metals, reflected by their superior activity, selectivity, and stability.[3,8−14]

However, the limited availability and unpredictable market price fluctuations of Pd present major issues for its implementation, particularly because many other established industrial processes continue to increase demand upon waning global Pd reserves. As such, the development of cheaper catalysts with improved Pd atom utilization and efficiency is of timely importance. It is often not practical to simply shift away from Pd-based catalysts and utilize more earth-abundant metals because doing so may require a completely new infrastructure, which is not cost-effective on an industrial scale. Instead, one common compromise strategy involves the synthesis of more economically practicable catalysts,[15] which remain directly compatible with existing infrastructure (*i.e.*, "drop-in" technologies) *via* the dilution of Pd with cheaper, more earth-abundant metals—often in the form of alloys. Importantly, this also provides access to unique synergistic effects (*e.g.*, ligand,[16] ensemble, and geometric effects[17]) that are intrinsic to alloys and can result in more efficient catalyst materials compared to the corresponding monometallic components.[17−20] This approach has been studied widely for a range of binary metal alloy catalysts in both bulk form and as well-defined nanoparticles (NPs).

Structurally well-defined ternary (*i.e.*, three-component) alloy NP catalysts are much less common and have not been widely studied for practical applications. Ternary alloys theoretically provide access to the abovementioned synergistic effects and offer finer tunability of surface reactivity, compared to bimetallic alloys. Examples of the controlled synthesis of binary nanoalloys from molecular precursors are increasingly numerous; there are also a limited but growing number of interesting reports of the preparation of so-called "high entropy alloys", based on several metals forming a single phase, albeit with limited control over composition.[21] By comparison, the synthesis of compositionally controlled ternary systems remain comparatively uncommon, particularly for combinations of metals that have disparate reduction potentials, which present inherent difficulties in achieving spontaneous co-reduction using a simple and convenient polyol-type approach.[22] While changes in the average sizes of bi- and trimetallic NPs could impact their final compositions, our focus in this study was to obtain compositionally tunable PdCu and PdAuCu alloy NPs

https://doi.org/10.1021/acscatal.3c01676
ACS Catal. 2023, 13, 11945−11953

of similar sizes, using microwave-assisted synthesis.[23−25] The incorporation of multiple metal atoms into a single, homogeneous phase is inhibited by disparate rates of reduction of ionic precursors in solution-based syntheses. Usually, such issues result in the formation of inhomogeneous (*i.e.*, phase-segregated) or core−shell structures.[26,27] Thus, the development of unconventional synthetic routes that are amenable to eventual synthesis at-scale, as well as a judicious selection of chemical precursors, reducing agents, and reaction conditions (*i.e.*, temperature, pressure, solvent system, *etc.*) are vital to the discovery of new nanocatalysts.

Among many novel synthetic approaches developed thus far, microwave-assisted heating has been shown by our group and others to be highly effective in synthesizing metastable alloy NPs based on combinations of classically immiscible metals, which are difficult to obtain using conventional (convective) heating methods.[17−20,28,29] Under microwave irradiation, polar solvent molecules and ionic metal precursors strongly couple with the oscillating electromagnetic field, leading to rapid, localized heat dissipation.[30−33] This nonuniform heating results in the generation of so-called "hotspots", whereby microscopic regions of a bulk solution can become superheated for short periods of time, compared to the bulk.[34,35] These regions are believed to provide unique environments to facilitate fast nucleation events under extreme conditions, including forced coreduction of different metal ions with dissimilar chemical reduction potentials.

Here, we present the syntheses of well-defined ternary PdAuCu NPs with controllable compositions and randomly alloyed (*i.e.*, solid-solution) structures using microwave-assisted heating. A systematic comparison of the experimental catalytic aqueous NO_2^- reduction activities of these novel nanostructures versus the related binary alloy NP systems (PdCu and PdAu) proves that the ternary alloys offer a greater degree of tunability. Importantly, the ternary alloy NPs are no less stable under identical operating conditions, and from an economic perspective, ternary PdAuCu NPs with optimized compositions displayed the best price-to-activity ratios, surpassing both PdCu and PdAu binary alloy NPs. This fundamental work underlines the significant longer-term potential of these (and other) ternary alloy NPs as economically appealing future catalysts.

RESULTS AND DISCUSSION

The convenient and reproducible synthesis of PdAuCu alloy NPs was achieved by a microwave-assisted polyol method that was modified from that in our previous work. Briefly, common metal salt precursors (K_2PdCl_4, $HAuCl_4$, and $CuCl_2{\cdot}2H_2O$; with molar ratios defined by the target NP ratio, $Pd_xAu_{(50-x/2)}Cu_{(50-x/2)}$) were co-dissolved in ethylene glycol (EG) and injected directly into a preheated EG solution (at 150 °C) containing *poly*(vinylpyrrolidone) (PVP) and $NaBH_4$ inside a microwave cavity. The addition rate was strictly controlled to be 3.0 $mmol_{(Pd+Au+Cu)}$ h^{-1} by using a syringe pump. Immediate darkening of the reaction mixture was observed, suggesting the rapid formation of NPs. Upon completion of precursor addition, the suspension was further irradiated under rapid stirring for 30 min to ensure complete reduction and to permit size-focusing. The final products were then purified by cycles of precipitation and redispersion in mixed solvent systems, before being analyzed using various characterization techniques (see the Supporting Information for more details). In our initial studies, the molar Au/Cu precursor ratio was maintained at 1:1, while the Pd molar ratio was systematically varied. We attempted to prepare five distinct NP compositions corresponding to the notional target formula, $Pd_xAu_{(50-x/2)}Cu_{(50-x/2)}$, where x = 70, 60, 50, 40, and 30. Monometallic Pd, Au, and Cu NPs were also synthesized under otherwise identical reaction conditions for comparison purposes.

Powder X-ray diffraction (PXRD) patterns of the as-synthesized ternary NPs showed reflections corresponding to a single phase corresponding to a face-centered cubic (fcc) lattice structure, akin to what was observed for the pure Pd, Au, and Cu NPs (Figures 1A and S1). The center of each observed Bragg reflection was measured to lie between the index positions for monometallic Cu ($2\theta_{max}$ = 43.12°) and Au ($2\theta_{max}$ = 38.10°) and were quite close to those of Pd ($2\theta_{max}$ = 40.15°) (Figure S1). The experimental lattice constants for the synthesized PdAuCu NPs were in close agreement with the calculated values obtained using Vegard's law, indicative of the formation of a random alloy arrangement within $Pd_xAu_{(50-x/2)}Cu_{(50-x/2)}$NPs (Figure 1B). Unlike previously studied $Pd_xAu_{(100-x)}$ NPs, which show a significant overall shift in the measured *d*-spacings as a function of x, the observed change of lattice constant for the $Pd_xAu_{(50-x/2)}Cu_{(50-x/2)}$NPs with respect to the value of x was less pronounced.[17] This is to be expected because the lattice constant of Pd (3.89 Å) is close to the average constant for Cu and Au (3.84 Å).[36] Measured peak widths at half-maximum were also similar for all five compositions, indicating comparable average crystallite domain sizes across the entire composition range studied. The actual compositions of all NPs were determined by digestion of samples in aqua regia followed by inductively coupled plasma optical emission spectroscopy (ICP-OES) analysis, which revealed only minor inconsistencies compared to the initial target ratios: in all cases, the actual measured values of $Pd_xAu_{(50-x/2)}Cu_{(50-x/2)}$ deviated by $\leq$ 4% compared to the notional target compositions (see Supporting Information, Table S1). This indicates that a given desired composition of PdAuCu NPs can be accurately and conveniently determined simply based on the metal salt precursor molar ratios. Henceforth, the ICP-derived values, x, y, and z (corresponding to $Pd_xAu_yCu_z$), are used when referring to specific NP compositions. It is also worth noting that the Au composition was found to be uniformly slightly higher (*i.e.*, 2−6 wt %) than the Cu composition, possibly due to the higher reduction potential of Au^{3+}/Au^0 (1.50 V) than Cu^{2+}/Cu^0 (0.34 V), which could favor faster incorporation of Au atoms into the growing PdAuCu NP seeds.[37]

Transmission electron microscopy (TEM) images of the as-synthesized PdAuCu NPs suggest that most of the NPs adopt an isotropic spherical (*i.e.*, cuboctahedral) morphology, with average diameters between 2 and 4 nm (Figures 1C and S2). Individual size distributions were obtained by measuring at least 250 individual particles for each composition. The capping agent PVP is known to favor isotropic NP growth, since it does not show a strong binding preference for any particular surface structure [*i.e.*, (111) *vs* (100)] and is therefore not usually effective in directing epitaxial growth of fcc metal NPs. Monometallic Pd NPs prepared by the same method were also cuboctahedral but with a larger average diameter of 6.7 ± 1.0 nm (Figure S3). Monometallic Au NPs prepared by the same method were much larger in size (20−30 nm) and displayed a greater morphological variation (Figure S4). In contrast, monometallic Cu NPs displayed irregular

https://doi.org/10.1021/acscatal.3c01676
ACS Catal. 2023, 13, 11945−11953

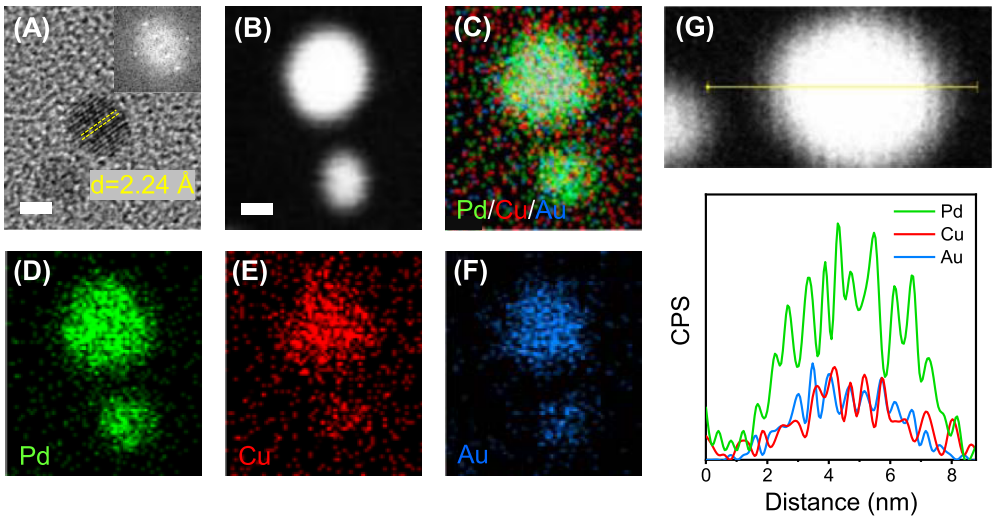

Figure 2. (A) Representative HRTEM image of $Pd_{52}Au_{26}Cu_{22}$NP with the lattice fringes shown with yellow dashed lines. Scale bar equals 2 nm. Inset: corresponding FFT. (B) HAADF-STEM image of two $Pd_{52}Au_{26}Cu_{22}$NPs. Scale bar equals 2 nm. (C−F) 2D EDS mappings of (C) overlay; (D) Pd; (E) Cu; and (F) Au signal. (G) Line scan profile of a $Pd_{52}Au_{26}Cu_{22}$NP with corresponding elemental counts.

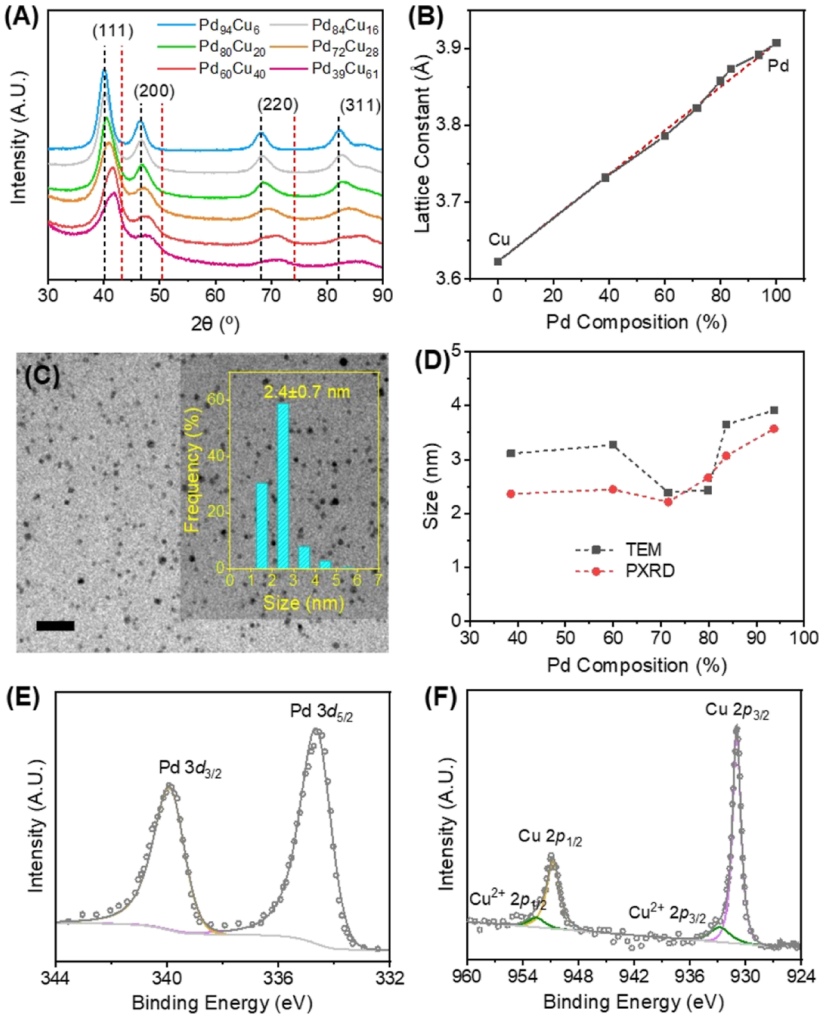

Figure 3. (A) PXRD patterns for PdCuNPs of various compositions. The standard reflection positions for Pd (black dashed line) and Cu (magenta dashed line) are also shown for reference. (B) Vegard's plot showing lattice constants of PdCuNPs as a function of Pd composition. (C) TEM image of $Pd_{72}Cu_{28}$NPs. Scale bar equals to 20 nm. Inset: size distribution histograph. (D) Particle size obtained from TEM analysis and PXRD reflection broadness as a function of Pd composition. (E) Pd 3d and (F) Cu 2p XPS spectra of $Pd_{72}Cu_{28}$NPs.

https://doi.org/10.1021/acscatal.3c01676
ACS Catal. 2023, 13, 11945−11953

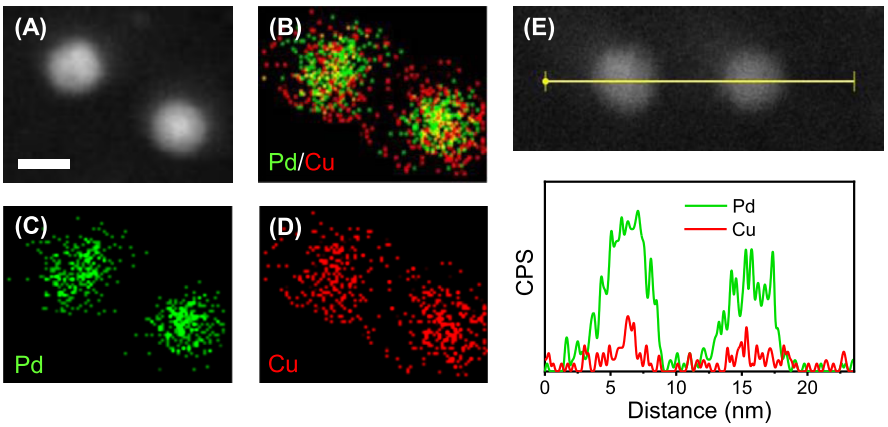

Figure 4. (A) HAADF-STEM image of two $Pd_{72}Cu_{28}$NPs. Scale bar equals to 5 nm. (B–D) 2D EDS mapping of (B) overlay; (C) Pd, and (D) Cu signal. (E) Line scan profile of two $Pd_{72}Cu_{28}$NPs with corresponding elemental counts.

geometries and a bimodal size distribution, with a prevalence of smaller (26 ± 9 nm) NPs and a minority of very large NPs with diameters over 100 nm (Figure S5). Taken together, our microwave-assisted synthetic method is clearly well-optimized for the formation of the target binary and ternary alloys but is not as well suited to the formation of monometallic species. It also confirms (at least qualitatively) that the alloying of two or three metals is important in the formation of small and near-monodisperse NPs under these reaction conditions.

The surface chemical states of the various NP compositions were studied by X-ray photoelectron spectroscopy (XPS). The Pd 3d and Au 4f binding energies were measured to be 334.7 and 83.1 eV, respectively, which matched precisely with the values corresponding to Pd^0 and Au^0 from previous reports (Figure 1D,E), with no evidence of these metals in more highly oxidized states.[37] On the other hand, a minority (*ca.* 14%) of Cu^{2+} (E_B = 932.9 eV) was detected in addition to the Cu^0 peak at 931.1 eV in the ternary NPs. Spin–orbit splitting values for the peak positions for Pd ($3d_{5/2}$ and $3d_{3/2}$), Au ($4f_{7/2}$ and $4f_{5/2}$), and Cu ($2p_{3/2}$ and $2p_{1/2}$) are 5.3, 3.7, and 19.9 eV, respectively, which agree well with theoretical values. Heteroatomic synergy between Pd and Au is also evident from the XPS peak positions, where charge transfer from Pd to Au leads to lower E_B values for Au, manifested as a downshift of 0.9 eV.[38] Cu is more easily oxidized by atmospheric oxygen during purification steps; therefore, it is suspected that the residual Cu^{2+} was caused by oxidation of surface (or near-surface) Cu atoms in the alloy NPs (Figure 1F). Furthermore, because Cu^0 and Cu^+ have identical binding energies, Auger spectroscopy was also employed to more accurately identify the potential range of oxidation states of Cu present in the ternary alloy NPs. The Cu-LMM Auger line (E_k = 918.8 eV) confirmed that the non-Cu^{2+} sites within PdAuCu NPs were only present in the Cu^0 state (Figure S6).[39]

Figure 2A shows a HRTEM image of a representative 3.5 nm cuboctahedral $Pd_{52}Au_{26}Cu_{22}$ NP with defined lattice fringes. The lattice *d*-spacing measured from the HRTEM image and fast Fourier transformation (FFT) was 0.224 nm, which corresponds closely to the {111} plane and is in direct agreement with the PXRD results (Figure 2A). Additionally, high-angle annular dark field scanning TEM (HAADF-STEM) imaging (Figure 2B), 2D-energy dispersive spectroscopy (EDS) mapping (Figure 2C–F), and EDS line scan profiling (Figure 2G) show no metallic heterogeneity or segregation of any element throughout the NPs. Overall, our combined characterizations confirmed the homogeneous mixing of Pd, Au, and Cu within ternary NPs of various compositions, indicating broad miscibility of the classically unstable Pd–Au–Cu system on the nanoscale. It is worth noting that, unlike PdAu, the PdCu system does not usually exist in bulk as a disordered fcc phase over all compositions, below 600 °C.[36] In contrast, the AuCu system is known to form the ordered intermetallic phases, Au_3Cu, AuCu, and $AuCu_3$, at 240, 410, and 390 °C, respectively.[37,38] Lastly, due to the similarly sized PdAuCu alloy NPs in our case and metals being primarily observed in the 0 oxidation states using XPS, ICP obtained loading values can be accurately used to determine the catalytic activity of these NPs. While some heterogeneity and segregation of the metals in these alloys cannot be entirely ruled out, such regions are not expected to play any measurable role in the observed catalytic activities.[40]

To facilitate more informative comparative structural and catalytic studies, binary PdCu NPs were prepared using the same microwave-assisted method. The PXRD patterns (Figure 3A) and corresponding Vegard plots (Figure 3B) clearly confirmed that Pd_xCu_{100-x} NPs could be prepared over a range of compositions (x = 39–94). Comprehensive structural characterization by TEM (Figures 3C,D and S7), XPS (Figures 3E,F and S8) and EDS (Figures 4 and S9, S10) collectively suggest that the binary PdCu NPs have similar morphologies, particle size, surface chemical states, and were homogeneously alloyed, as with the ternary PdAuCu NPs. ICP-OES analysis of the six distinct Pd_xCu_{100-x} alloy NPs showed slightly higher than expected (targeted) values of Pd/Cu. PXRD analyses of the PdCu NPs also showed that the reflection positions were tunable, as observed for PdAuCu NPs. For instance, the <111> reflection for Cu-rich $Pd_{39}Cu_{61}$ NPs was closest to the pure Cu reference, as shown by its relation to the Cu reference (dashed magenta line; Figure 3A). Conversely, peak positions for $Pd_{94}Cu_6$ matched very well with pure Pd; these observations are also in agreement with the corresponding Vegard plot (Figure 3B), wherein measured lattice constants for all PdCu alloys showed a linear increase upon increasing the Pd content. TEM measurements confirm that the PdCu alloy NPs are also near-monodisperse with average diameters ranging between 2 and 4 nm (Figure 3D), with the outlying Pd- and Cu-rich compositions tending to be larger than intermediate compositions. XPS and Auger analyses further confirmed that only Pd^0 was observed in PdCu NPs while Cu existed primarily as Cu^0 with small amounts of Cu^{2+} also detected.

https://doi.org/10.1021/acscatal.3c01676
ACS Catal. 2023, 13, 11945–11953

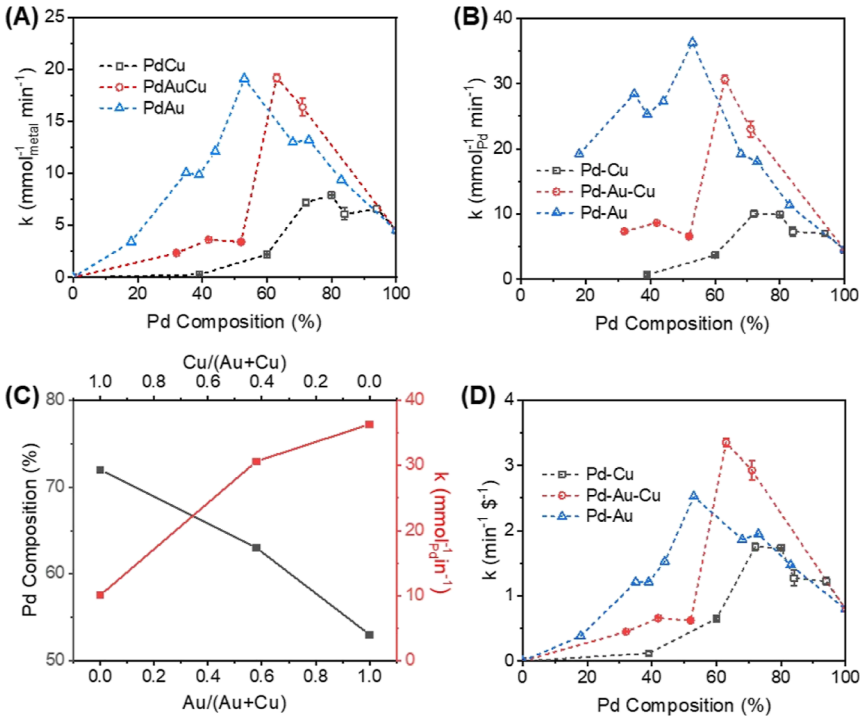

Figure 5. (A) Rate constants normalized by total metal as a function of Pd composition. (B) Rate constants normalized by Pd content plotted *vs* Pd composition. (C) Pd composition at which activity maxima was achieved and corresponding rate constants as a function of Cu and Au fractions. (D) Rate constants normalized by the cost of catalysts for PdCu/*a*-SiO_2, PdAu/*a*-SiO_2, and PdAuCu/*a*-SiO_2 catalysts with different compositions.

Lastly, homogeneous distribution and alloying of Pd and Cu was confirmed using HRTEM-EDS analysis (Figures 4 and S10).

To enable model aqueous NO_2^- reduction reaction studies, various PdAuCu and PdCu NPs were dispersed onto amorphous silica (*a*-SiO_2) by direct impregnation in H_2O/EtOH, followed by filtration and drying under vacuum, to yield composite catalysts with 1−2 wt % total metal loading (see the Supporting Information). TEM imaging shows that the NPs were spatially well separated after loading without detectable structural changes. Pseudo-first-order kinetic parameters were obtained, and up to 80% NO_2^- conversion was observed in all cases. Log concentrations versus time plots for SiO_2-supported PdCu and PdAuCu NPs are presented in Figures S15 and S16. Analogous data for SiO_2-supported PdAu NPs are available in a previously published report for these bimetallics.[11] To ascertain the composition-dependent activities of the NPs as a direct function of composition, the experimentally measured first-order rate constants were normalized based on the total metal loading values determined by ICP-OES (Table S1). A composition dependence plot was derived by plotting the normalized activities of various $Pd_xAu_yCu_z$/*a*-SiO_2 catalysts as a function of Pd composition; a maximum was identified for $Pd_{63}Au_{16}Cu_{13}$/*a*-SiO_2 (19.19 $mmol_{metal}^{-1}$ min^{-1}). Notably, this catalyst also significantly outperformed the "conventional", monometallic Pd/*a*-SiO_2 catalyst (4.54 $mmol_{metal}^{-1}$ min^{-1}), while requiring 37% less Pd (Figure 5A; red data). Moreover, monometallic Au and Cu NPs supported on the same *a*-SiO_2 support did not show any detectable NO_2^- reduction activity. Taken together, these observations provide direct evidence that enhanced the catalytic activity results from synergistic alloying effects between Pd, Au, and Cu.

When considering the Au-free PdCu/*a*-SiO_2 binary catalyst system, the corresponding activity−composition curve also revealed a maximum NO_2^- reduction activity for intermediate Pd/Cu compositions (Figure 5A; black data). The most Pd-rich catalyst studied ($Pd_{80}Cu_{20}$) also showed a markedly higher catalytic activity than that for monometallic Pd/*a*-SiO_2 (7.91 $mmol_{metal}^{-1}$ min^{-1}) (Figure 5A).

By directly comparing the catalytic performances of PdAuCu, PdCu, and the previously reported PdAu NPs, it is clear that Au is more effective than Cu in promoting intrinsic activity per Pd site.[17] The ability to synthetically continuously tune the Au/Cu ratios in the ternary alloys as a means to adjust the catalytic activity is underlined by the fact that PdAuCu catalysts show activities intermediate between the bimetallic PdAu and PdCu systems. Specifically, the highest measured activities (normalized by at % Pd) were 36.32, 30.64, and 10.07 $mmol_{Pd}^{-1}$ min^{-1}, corresponding to 53, 63, and 72 at % Pd, respectively, for PdAu, PdAuCu, and PdCu systems (Figure 5B,C). From an economic standpoint, the use of PdCu and PdAuCu nanoalloys is most enticing because Cu is orders of magnitude cheaper ($0.006 g^{-1}) than Pd ($53.58 g^{-1}) or Au ($49.15 g^{-1}) (Macrotrends; average price in 2019). Therefore, when the measured activity is normalized by the cost of the catalysts and plotted as a function of composition, some interesting conclusions can be drawn (Figure 5D). $Pd_{63}Au_{22}Cu_{16}$/*a*-SiO_2 has the highest price−performance activity of 3.353 min^{-1} $^{-1}$, which is higher than that of either $Pd_{53}Au_{47}$ (2.527 min^{-1} $^{-1}$) or $Pd_{72}Cu_{28}$ catalysts (1.753 min^{-1} $^{-1}$). It is critical to fully understand the selectivity of aqueous phase NO_2^- reduction by using these ternary PdAuCu alloy systems. Figure S11A shows the ammonia selectivity of PdAuCuNPs, ranging from 0.87 to 26% with increasing Cu contents and decreasing Pd contents. The remaining product is assumed to be N_2 as shown in Scheme 1 and the literature.[12] Our previous study showed near quantitative (>98%) conversions of NO_2^- to N_2 using Pd_xAu_{100-x} nanoalloys,[11]

https://doi.org/10.1021/acscatal.3c01676
ACS Catal. 2023, 13, 11945−11953

whereas PdCuNPs showed increasing ammonia selectivity from 0.87 to 55% with increasing Cu contents (Figure S11B). The ratio between Cu and Pd contents within these nanoalloys seems to dictate the ammonia selectivity, at least partially. Finally, postcatalytic studies of the supported NP catalysts showed no noticeable structural changes, as confirmed by TEM (Figures S12 and 13) measurements.

Next, to better understand the relationship between the catalyst composition and apparent NO_2^- reduction activity, we employed density functional theory (DFT) calculations. Previous studies have shown that the atomic ensemble effects are predominant in determining NP surfaces' reactivity as compared to strain and electronic effects for alloys comprising strongly (*e.g.*, Pd) and weakly binding (*e.g.*, Au and Cu) metals.[18,41,42] Specific ensemble geometries and bulk NP compositions most accurately describe local adsorption environments for adsorbates,[43] which is of importance for understanding the origins of catalytic activities, *i.e.*, by ensuring one substrate or intermediate is not too strongly bound so that its release becomes a rate-determining step.[44−46] Thus, the activities of different alloy ensembles found on PdAu, PdCu, and PdAuCu surfaces were evaluated and compared using a 2D volcano activity model for NO_2^- reduction as a function of N and N_2 binding energies (Figure 6).[47] The reason why we used

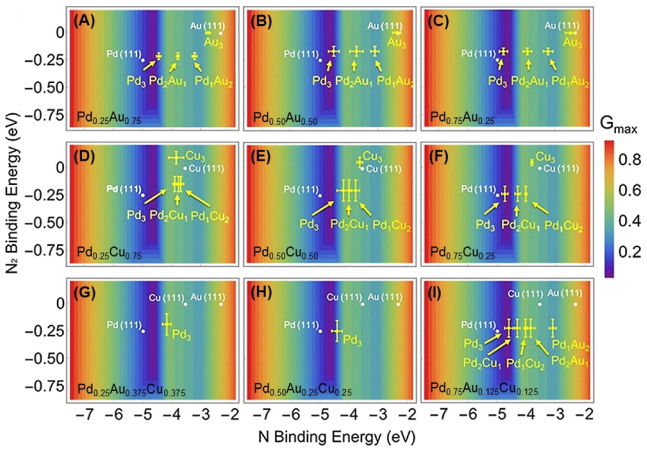

Figure 6. Volcano activity plot of nitrite reduction as a function of N and N_2 binding energies on (A) $Pd_{0.25}Au_{0.75}$; (B) $Pd_{0.50}Au_{0.50}$; (C) $Pd_{0.75}Au_{0.25}$; (D) $Pd_{0.25}Cu_{0.75}$; (E) $Pd_{0.50}Cu_{0.50}$; (F) $Pd_{0.75}Cu_{0.25}$; (G) $Pd_{0.25}Au_{0.375}Cu_{0.375}$; (H) $Pd_{0.50}Au_{0.25}Cu_{0.25}$; and (I) $Pd_{0.75}Au_{0.125}Cu_{0.125}$ surfaces. Random alloy models were used to evaluate the reactivity on PdAu, PdCu, and PdAuCu(111) surfaces. For each alloy composition, more than 15 randomly alloyed configurations were generated for DFT calculations. The error bars were calculated as the standard deviations of binding energies from 10 different random alloy geometries.

N and N_2 binding energies as the descriptors is that the N binding energy generally has good linear relationships with the binding energies of other reaction intermediates in nitrite reduction toward N_2 formation (except the N_2 binding energy), which was proven by our previous work[47] and also discussed in a recent review.[48] Therefore, once we know the N and N_2 binding energies, we can quickly estimate the reaction energetics based on the previously identified linear relations.[47] The rate-determining step of the left side of the volcano is NO direct dissociation, while that of the right side of the volcano is rate-limited by NO dissociation after hydrogenation. More modeling details can be found in the Supporting Information.

This volcano model has shown high accuracy for predicting the nitrite reduction performance of various mono-, bi-,[49] and trimetallic[50] systems. Unlike Pd(111) surfaces, pure Au(111) and Cu(111) surfaces adsorb N too weakly to be active, which is in agreement with the experimental observation that monometallic Au and Cu NPs are inert for NO_2^- reduction. In contrast, (111) surfaces for PdAuCu ternary alloys present a statistical variation of M_3 ensembles (*i.e.*, Pd_3, Pd_2Au, Pd_2Cu, PdAuCu, $PdAu_2$, $PdCu_2$, Au_2Cu, $AuCu_2$, Au_3, and Cu_3) as a function of $Pd_xAu_yCu_z$, at which N and N_2 will have different binding energies. DFT provides a means to examine these more complicated systems by providing average binding energies. Pd_3 triatomic ensembles are the most strongly adsorbing sites, with binding energies that reside closer to the "volcano peak" (meaning, the theoretical optimum) compared to other possible ensembles. However, alloying different amounts of Au, Cu, or both Au and Cu into a Pd surface enables tuning of the activities of Pd_3 ensembles, making them more active compared to monometallic Pd(111) at certain compositions; this is due to electronic effects that extend beyond individual Pd_3 ensembles on the NP surfaces. As shown in Figure 6, Pd_3 sites at the surfaces of $Pd_{0.50}Au_{0.50}$, $Pd_{0.75}Cu_{0.25}$, and $Pd_{0.75}Au_{0.125}Cu_{0.125}$ lie at the volcano peak, suggesting that NPs of such compositions are the most active in each family. This calculation qualitatively matches our experimental catalysis results (Figure 5). Due to the high computational cost for sampling many different ensemble surfaces, we evaluated all the possible triatomic ensembles on PdAu and PdCu but only the most notable ensembles on PdAuCu. PdAuCu trimers are not active due to the too-weak binding to the adsorbate, and it is far away from the volcano peak. Therefore, we did not include PdAuCu trimers in our DFT calculations. To summarize our results, alloying of Au and/or Cu into Pd is found to optimize the NO_2^- reduction activity of Pd-rich sites (*e.g.*, the 3-fold Pd_3 site) by slightly weakening its N-bonding, which is due to the synergetic contribution of strain and electronic effects originated from the differences in the lattice constant and work function among Pd, Au, and Cu.

CONCLUSIONS

In conclusion, ternary PdAuCu NPs with controllable compositions were prepared using a microwave-assisted polyol method with the aid of $NaBH_4$ as a secondary reducing agent. Thorough structural characterization confirmed that $Pd_xAu_yCu_z$ NPs with various compositions all exist as homogeneously alloyed (or solid-solution) structures. PdAuCu NPs and binary PdCuNPs synthesized using the same programmable method were supported on amorphous silica and were found to be both highly active and stable in aqueous nitrite reduction using H_2 gas as the reductant. The comparative catalytic activities of both PdCu and PdAuCu catalysts were found to be superior to previously studied PdAu nanocatalysts, as well as monometallic Pd. DFT calculations suggest that alloying Au, Cu, or both Au and Cu with Pd leads to improved performance for optimized compositions due to the weakened binding energies of the most highly active Pd_3 triatomic ensembles, which were found to have more favorable N-binding energy compared to monometallic Pd(111) surfaces. More interestingly, we show that the activities can be tuned by adjusting the ratio of Au to Cu in the alloy. From an economic standpoint, the ternary NPs show significantly better price-to-activity ratios than binary analogues of PdAu

https://doi.org/10.1021/acscatal.3c01676
ACS Catal. 2023, 13, 11945−11953

and PdCu systems, lending promise to the development of such novel ternary alloy systems for future applications at scale.

■ ASSOCIATED CONTENT

Supporting Information

The Supporting Information is available free of charge at https://pubs.acs.org/doi/10.1021/acscatal.3c01676.

Detailed experimental methods, PXRD patterns, TEM images, HRTEM images, EDS mapping, Cu Auger spectra for PdCu and PdAuCuNPs, TEM images for catalysts after nitrite reduction, additional catalysis, and DFT information (PDF)

■ AUTHOR INFORMATION

Corresponding Authors

Graeme Henkelman − *Department of Chemistry, The University of Texas at Austin, Austin, Texas 78712-1224, United States; Texas Materials Institute, The University of Texas at Austin, Austin, Texas 78712-1591, United States;* orcid.org/0000-0002-0336-7153; Email: werth@utexas.edu

Charles J. Werth − *Department of Civil, Architectural and Environmental Engineering, The University of Texas at Austin, Austin, Texas 78712, United States;* orcid.org/0000-0002-8492-5523; Email: henkelman@utexas.edu

Simon M. Humphrey − *Department of Chemistry, The University of Texas at Austin, Austin, Texas 78712-1224, United States; Texas Materials Institute, The University of Texas at Austin, Austin, Texas 78712-1591, United States;* orcid.org/0000-0001-5379-4623; Email: smh@cm.utexas.edu

Authors

Pranaw Kunal − *Department of Chemistry, The University of Texas at Austin, Austin, Texas 78712-1224, United States;* Present Address: Ames Laboratory, 15 Spedding Hall, 2416 Pammel Dr, Ames, IA, 50011, USA; orcid.org/0000-0002-1647-242X

Chenxu Yan − *Department of Civil, Architectural and Environmental Engineering, The University of Texas at Austin, Austin, Texas 78712, United States;* Present Address: Carollo Engineers. 8911 N Capital of Texas Hwy Suite 2200, Austin, TX 78759, USA.; orcid.org/0000-0002-2227-5510

Hongyu Guo − *Department of Chemistry, The University of Texas at Austin, Austin, Texas 78712-1224, United States;* Present Address: School of Materials Science and Engineering, Peking University, Beijing 100871, China.

Hao Li − *Department of Chemistry, The University of Texas at Austin, Austin, Texas 78712-1224, United States;* Present Address: Advanced Institute for Materials Research (WPI-AIMR), Tohoku University, Sendai 980-8577, Japan.; orcid.org/0000-0002-7577-1366

Carolyn E. Brady − *Department of Chemistry, The University of Texas at Austin, Austin, Texas 78712-1224, United States; Department of Civil, Architectural and Environmental Engineering, The University of Texas at Austin, Austin, Texas 78712, United States*

Michael Duncan − *Department of Chemistry, The University of Texas at Austin, Austin, Texas 78712-1224, United States*

Xun Zhan − *Texas Materials Institute, The University of Texas at Austin, Austin, Texas 78712-1591, United States*

Complete contact information is available at: https://pubs.acs.org/10.1021/acscatal.3c01676

Author Contributions

[▽]P.K. and C.Y. contributed equally.

Notes

The authors declare no competing financial interest.

■ ACKNOWLEDGMENTS

The authors thank Dr. Hugo Celio (XPS) for the analytical assistance. The funding of this work was provided by the National Science Foundation under grant no. CHE-2109120 and the Welch Foundation (F-1738 and F-1841).

■ REFERENCES

(1) Burow, K. R.; Nolan, B. T.; Rupert, M. G.; Dubrovsky, N. M. Nitrate in Groundwater of the United States, 1991−2003. *Environ. Sci.* **2010**, *44*, 4988−4997.

(2) Kapoor, A.; Viraraghavan, T. Nitrate Removal From Drinking Water—Review. *J. Environ. Eng.* **1997**, *123*, 371−380.

(3) Pintar, A.; Batista, J.; Levec, J.; Kajiuchi, T. Kinetics of the Catalytic Liquid-Phase Hydrogenation of Aqueous Nitrate Solutions. *Appl. Catal., B* **1996**, *11*, 81−98.

(4) Weyer, P. J.; Cerhan, J. R.; Kross, B. C.; Hallberg, G. R.; Kantamneni, J.; Breuer, G.; Jones, M. P.; Zheng, W.; Lynch, C. F. Municipal Drinking Water Nitrate Level and Cancer Risk in Older Women: The Iowa Women's Health Study. *Epidemiology* **2001**, *12*, 327−338.

(5) Comly, H. H. Cyanosis in Infants Caused by Nitrates in Well Water. *J. Am. Med. Assoc.* **1945**, *129*, 112−116.

(6) Issenberg, P. Nitrite, Nitrosamines, and Cancer. *Fed. Proc.* **1976**, *35*, 1322−1326.

(7) Elimelech, M.; Phillip, W. A. The Future of Seawater Desalination: Energy, Technology, and the Environment. *Science* **2011**, *333*, 712−717.

(8) Chaplin, B. P.; Shapley, J. R.; Werth, C. J. Regeneration of Sulfur-Fouled Bimetallic Pd-Based Catalysts. *Environ. Sci. Technol.* **2007**, *41*, 5491−5497.

(9) Xie, Y.; Cao, H.; Li, Y.; Zhang, Y.; Crittenden, J. C. Highly Selective PdCu/Amorphous Silica-Alumina (ASA) Catalysts for Groundwater Denitration. *Environ. Sci. Technol.* **2011**, *45*, 4066−4072.

(10) Guy, K. A.; Xu, H.; Yang, J. C.; Werth, C. J.; Shapley, J. R. Catalytic Nitrate and Nitrite Reduction with Pd−Cu/PVP Colloids in Water: Composition, Structure, and Reactivity Correlations. *J. Phys. Chem. C* **2009**, *113*, 8177−8185.

(11) Seraj, S.; Kunal, P.; Li, H.; Henkelman, G.; Humphrey, S. M.; Werth, C. J. PdAu Alloy Nanoparticle Catalysts: Effective Candidates for Nitrite Reduction in Water. *ACS Catal.* **2017**, *7*, 3268−3276.

(12) Chaplin, B. P.; Reinhard, M.; Schneider, W. F.; Schüth, C.; Shapley, J. R.; Strathmann, T. J.; Werth, C. J. Critical Review of Pd-Based Catalytic Treatment of Priority Contaminants in Water. *Environ. Sci. Technol.* **2012**, *46*, 3655−3670.

(13) Shuai, D.; Choe, J. K.; Shapley, J. R.; Werth, C. J. Enhanced Activity and Selectivity of Carbon Nanofiber Supported Pd Catalysts for Nitrite Reduction. *Environ. Sci. Technol.* **2012**, *46*, 2847−2855.

(14) Chen, M.; Kumar, D.; Yi, C. W.; Goodman, D. W. The Promotional Effect of Gold in Catalysis by Palladium−Gold. *Science* **2005**, *310*, 291−293.

(15) Werth, C. J.; Yan, C.; Troutman, J. P. Factors Impeding Replacement of Ion Exchange with (Electro)Catalytic Treatment for Nitrate Removal From Drinking Water. *ACS EST Engg* **2021**, *1* (1), 6−20.

(16) Asano, M.; Kawamura, R.; Sasakawa, R.; Todoroki, N.; Wadayama, T. Oxygen Reduction Reaction Activity for Strain-Controlled Pt-Based Model Alloy Catalysts: Surface Strains and

Direct Electronic Effects Induced by Alloying Elements. *ACS Catal.* **2016**, *6*, 5285−5289.
(17) Kunal, P.; Li, H.; Dewing, B. L.; Zhang, L.; Jarvis, K.; Henkelman, G.; Humphrey, S. M. Microwave-Assisted Synthesis of Pd_xAu_{100-x} Alloy Nanoparticles: A Combined Experimental and Theoretical Assessment of Synthetic and Compositional Effects upon Catalytic Reactivity. *ACS Catal.* **2016**, *6*, 4882−4893.
(18) Guo, H.; Li, H.; Jarvis, K.; Wan, H.; Kunal, P.; Dunning, S. G.; Liu, Y.; Henkelman, G.; Humphrey, S. M. Microwave-Assisted Synthesis of Classically Immiscible Ag−Ir Alloy Nanoparticle Catalysts. *ACS Catal.* **2018**, *8*, 11386−11397.
(19) Guo, H.; Li, H.; Fernandez, D.; Willis, S.; Jarvis, K.; Henkelman, G.; Humphrey, S. M. Stabilizer-Free CuIr Alloy Nanoparticle Catalysts. *Chem. Mater.* **2019**, *31*, 10225−10235.
(20) Guo, H.; Fang, Z.; Li, H.; Fernandez, D.; Henkelman, G.; Humphrey, S. M.; Yu, G. Rational Design of Rhodium−Iridium Alloy Nanoparticles as Highly Active Catalysts for Acidic Oxygen Evolution. *ACS Nano* **2019**, *13*, 13225−13234.
(21) Dey, G. R.; McCormick, C. R.; Soliman, S. S.; Darling, A. J.; Schaak, R. E. Chemical Insights into the Formation of Colloidal High Entropy Alloy Nanoparticles. *ACS Nano* **2023**, *17* (6), 5943−5955.
(22) Fiévet, F.; Ammar-Merah, S.; Brayner, R.; Chau, F.; Giraud, M.; Mammeri, F.; Peron, J.; Piquemal, J.-Y.; Sicard, L.; Viau, G. The Polyol Process: a Unique Method for Easy Access to Metal Nanoparticles with Tailored Sizes, Shapes and Compositions. *Chem. Soc. Rev.* **2018**, *47*, 5187−5233.
(23) He, Q.; Miedziak, P. J.; Kesavan, L.; Dimitratos, N.; Sankar, M.; Lopez-Sanchez, J. A.; Forde, M. M.; Edwards, J. K.; Knight, D. W.; Taylor, S. H.; Kiely, C. J.; Hutchings, G. J. Switching-off toluene formation in the solvent-free oxidation of benzyl alcohol using supported trimetallic Au-Pd-Pt nanoparticles. *Faraday Discuss* **2013**, *162*, 365−378.
(24) Tiruvalam, R. C.; Pritchard, J. C.; Dimitratos, N.; Lopez-Sanchez, J. A.; Edwards, J. K.; Carley, A. F.; Hutchings, G. J.; Kiely, C. J. Aberration corrected analytical electron microscopy studies of sol-immobilized Au + Pd, Au{Pd} and Pd{Au} catalysts used for benzyl alcohol oxidation and hydrogen peroxide production. *Faraday Discuss* **2011**, *152*, 63−86.
(25) Agarwal, N.; Freakley, S. J.; McVicker, R. U.; Althahban, S. M.; Dimitratos, N.; He, Q.; Morgan, D. J.; Jenkins, R. L.; Willock, D. J.; Taylor, S. H.; Kiely, C. J.; Hutchings, G. J. Aqueous Au-Pd colloids catalyze selective CH4 oxidation to Ch3OH with O2 under mild conditions. *Science* **2017**, *358*, 223−227.
(26) Tsuji, M.; Matsunaga, M.; Yoshida, Y.; Hattori, M.; Ishizaki, T. Effects of Au Fraction on the Morphology and Stability of Au−Ag−Cu Trimetallic Particles Prepared Using a Polyol Method. *CrystEngComm* **2013**, *15*, 7062−7070.
(27) Liu, D.; Lu, S.; Xue, Y.; Guan, Z.; Fang, J.; Zhu, W.; Zhuang, Z. One-Pot Synthesis of IrNi@Ir Core-Shell Nanoparticles as Highly Active Hydrogen Oxidation Reaction Electrocatalyst in Alkaline Electrolyte. *Nano Energy* **2019**, *59*, 26−32.
(28) García, S.; Zhang, L.; Piburn, G. W.; Henkelman, G.; Humphrey, S. M. Microwave Synthesis of Classically Immiscible Rhodium−Silver and Rhodium−Gold Alloy Nanoparticles: Highly Active Hydrogenation Catalysts. *ACS Nano* **2014**, *8*, 11512−11521.
(29) Köhler, D.; Heise, M.; Baranov, A. I.; Luo, Y.; Geiger, D.; Ruck, M.; Armbrüster, M. Synthesis of BiRh Nanoplates with Superior Catalytic Performance in the Semihydrogenation of Acetylene. *Chem. Mater.* **2012**, *24*, 1639−1644.
(30) Dahl, J. A.; Maddux, B. L. S.; Hutchison, J. E. Toward Greener Nanosynthesis. *Chem. Rev.* **2007**, *107*, 2228−2269.
(31) Tsuji, M.; Hashimoto, M.; Nishizawa, Y.; Kubokawa, M.; Tsuji, T. Microwave-Assisted Synthesis of Metallic Nanostructures in Solution. *Chem.—Eur. J.* **2005**, *11*, 440−452.
(32) Dallinger, D.; Kappe, C. O. Microwave-Assisted Synthesis in Water as Solvent. *Chem. Rev.* **2007**, *107*, 2563−2591.
(33) Zhu, Y.-J.; Chen, F. Microwave-Assisted Preparation of Inorganic Nanostructures in Liquid Phase. *Chem. Rev.* **2014**, *114*, 6462−6555.
(34) Ma, Y.; Vileno, E.; Suib, S. L.; Dutta, P. K. Synthesis of Tetragonal $BaTiO_3$ by Microwave Heating and Conventional Heating. *Chem. Mater.* **1997**, *9*, 3023−3031.
(35) Baghbanzadeh, M.; Carbone, L.; Cozzoli, P. D.; Kappe, C. O. Microwave-Assisted Synthesis of Colloidal Inorganic Nanocrystals. *Angew. Chem., Int. Ed.* **2011**, *50*, 11312−11359.
(36) Gilroy, K. D.; Ruditskiy, A.; Peng, H.-C.; Qin, D.; Xia, Y. Bimetallic Nanocrystals: Syntheses, Properties, and Applications. *Chem. Rev.* **2016**, *116*, 10414−10472.
(37) Tarditi, A. M.; Imhoff, C.; Miller, J. B.; Cornaglia, L. Surface Composition of PdCuAu Ternary Alloys: A Combined LEIS and XPS Study. *Surf. Interface Anal.* **2015**, *47*, 745−754.
(38) Yi, C.-W.; Luo, K.; Wei, T.; Goodman, D. W. The Composition and Structure of Pd−Au surfaces. *JPCB* **2005**, *109* (39), 18535−18540.
(39) Liu, Y.; Chen, L.; Cheng, T.; Guo, H.; Sun, B.; Wang, Y. Preparation and Application in Assembling High-Performance Fuel Cell Catalysts of Colloidal PtCu Alloy Nanoclusters. *J. Power Sources* **2018**, *395*, 66−76.
(40) Zhang, K.; Way, J. D. Palladium-copper membranes for hydrogen separation. *Sep. Purif. Technol.* **2017**, *186*, 39−44.
(41) Li, H.; Evans, E. J.; Mullins, C. B.; Henkelman, G. Ethanol Decomposition on Pd−Au Alloy Catalysts. *J. Phys. Chem. C* **2018**, *122*, 22024−22032.
(42) Li, H.; Shin, K.; Henkelman, G. Effects of Ensembles, Ligand, and Strain on Adsorbate Binding to Alloy Surfaces. *J. Chem. Phys.* **2018**, *149*, 174705.
(43) Li, H.; Chai, W.; Henkelman, G. Selectivity for Ethanol Partial Oxidation: The Unique Chemistry of Single-Atom Alloy Catalysts on Au, Ag, and Cu(111). *J. Mater. Chem. A* **2019**, *7*, 23868−23877.
(44) Evans, E. J.; Li, H.; Han, S.; Henkelman, G.; Mullins, C. B. Oxidative Cross-Esterification and Related Pathways of Co-Adsorbed Oxygen and Ethanol on Pd−Au. *ACS Catal.* **2019**, *9*, 4516−4525.
(45) Li, H.; Henkelman, G. Dehydrogenation Selectivity of Ethanol on Close-Packed Transition Metal Surfaces: A Computational Study of Monometallic, Pd/Au, and Rh/Au Catalysts. *J. Phys. Chem. C* **2017**, *121*, 27504−27510.
(46) Evans, E. J.; Li, H.; Yu, W.-Y.; Mullen, G. M.; Henkelman, G.; Mullins, C. B. Mechanistic Insights on Ethanol Dehydrogenation on Pd−Au Model Catalysts: A Combined Experimental and DFT Study. *Phys. Chem. Chem. Phys.* **2017**, *19*, 30578−30589.
(47) Li, H.; Guo, S.; Shin, K.; Wong, M. S.; Henkelman, G. Design of a Pd-Au Nitrite Reduction Catalyst by Identifying and Optimizing Active Ensembles. *ACS Catal.* **2019**, *9*, 7957−7966.
(48) Yang, G.; Zhou, P.; Liang, J.; Li, H.; Wang, F. Opportunities and challenges in aqueous nitrate and nitrite reduction beyond electrocatalysis. *Inorg. Chem. Front.* **2023**, *10*, 4610−4631.
(49) Troutman, J. P.; Li, H.; Haddix, A. M.; Kienzle, B. A.; Henkelman, G.; Humphrey, S. M.; Werth, C. J. PdAg Alloy Nanocatalysts: Toward Economically Viable Nitrite Reduction in Drinking Water. *ACS Catal.* **2020**, *10*, 7979−7989.
(50) Guo, S.; Li, H.; Heck, K. N.; Luan, X.; Guo, W.; Henkelman, G.; Wong, M. Gold boosts nitrate reduction and deactivation resistance to indium-promoted palladium catalysts. *Applied Catal. B. Environ.* **2022**, *305* (15), 121048.

https://doi.org/10.1021/acscatal.3c01676
ACS Catal. 2023, 13, 11945−11953